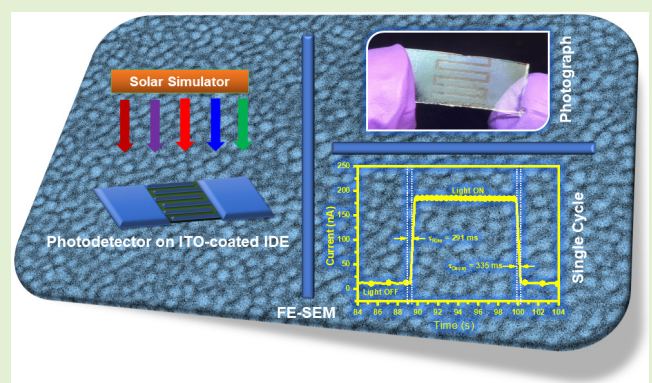# Unraveling the Properties of Interdigital Electrode-Based $\gamma$-In$_2$Se$_3$ Photodetectors for Optimal Performance

Yogesh Hase, Shruti Shah, Somnath Ladhane, Vidya Doiphode, Ashvini Punde, Pratibha Shinde, Swati Rahane, Dhanashri Kale, Bharat Bade, Ashish Waghmare, Mohit Prasad, Shashikant P. Patole[ID], and Sandesh Jadkar

***Abstract*—We successfully deposited In$_2$Se$_3$ films on the interdigital electrode (IDE) substrates using the radio frequency (RF)-magnetron sputtering method with optimized parameters. The formation of high-quality $\gamma$-In$_2$Se$_3$ using X-ray diffraction (XRD), Raman spectroscopy, X-ray photoelectron spectroscopy (XPS), field emission scanning electron microscopy (FE-SEM), and energy dispersive spectroscopy (EDS) is explored. Subsequently, we fabricated $\gamma$-In$_2$Se$_3$-based photodetectors on indium tin oxide (ITO)-coated IDE using optimized parameters. The detailed investigation focused on the influence of IDE spacing, bias voltage, and light intensity on the photodetector properties. The photodetector fabricated with an IDE spacing of 335 $\mu$m exhibited outstanding properties, including the highest photoresponsivity of 14.8 $\mu$A/W and detectivity of 31.3 × 10$^7$ Jones. It also demonstrated a fast rise time of 99 ms and a decay time of 61 ms. In the bias voltage variation study, the $\gamma$-In$_2$Se$_3$-based photodetectors exhibited a linear relationship between the change in current and the bias potential, indicating the formation of ohmic contact between $\gamma$-In$_2$Se$_3$ and ITO electrodes. Examining light intensity photoresponse, we varied the power density of light from 5 to 30 mW/cm$^2$. We observed a direct proportionality between the generated photocurrent and the incident light intensity. However, at higher light intensities, there was a decrease in photodetectivity from 3.97 × 10$^8$ to 1.16 × 10$^8$ Jones and a reduction in photoresponsivity from 33.36 to 9.73 $\mu$A/W for the $\gamma$-In$_2$Se$_3$-based photodetectors. In conclusion, the photodetector properties of $\gamma$-In$_2$Se$_3$-based devices are critically influenced by IDE spacing, bias voltage, and light intensity.

***Index Terms*—** $\gamma$-In$_2$Se$_3$, interdigital electrode (IDE), photodetector, radio frequency (RF) magnetron sputtering.

## I. INTRODUCTION

INDIUM selenide (In$_2$Se$_3$) is a member of the III–VI group of chalcogenides and has gained significant attention due to its attractive optoelectronic properties. Due to unique properties, In$_2$Se$_3$ thin films have been studied and explored for various applications such as solar cells [1], thermoelectric devices [2], gas sensors [3], field effect transistors [4], photoelectrochemical cells [5], batteries [6]. Furthermore, the material has been successfully employed in photodetector applications due to its tunable bandgap [7], high absorption coefficient [8], high photoresponsivity [9], and excellent stability [10]. Photodetectors are optical sensors that convert light energy into an electrical signal. The exciting performance of photodetectors can be achieved successfully by utilizing semiconductor materials with a high absorption coefficient, high carrier mobility, and relatively narrow bandgap. Two-dimensional van der Waals materials (vdWMs), such as graphene (Gr), borophene, elemental group VA members, transition metal dichalcogenides (TMDCs), group IIIA–VA, IIIA–VIA, IVA–VIA compounds, topological

insulators (TIs), perovskites, etc. [11], [12], are the most appealing and promising candidates for the next generation of high-performance photodetectors. The group III–VI compound semiconductors, In$_2$Se$_3$, offers several advantages over other cutting-edge materials in developing high-performance photodetectors. In$_2$Se$_3$ shows a tunable thickness-dependent optical bandgap ranging from 1.45 to 2.8 eV, chemical stability, high carrier mobility, and compatibility with flexible substrates, making it a promising candidate in photodetector application [13], [14], [15], [16]. It has a high absorption coefficient ($10^4$ cm$^{-1}$) in the visible range and efficiently generates electron–hole pairs on photoexcitation [17], [18]. Different methods have been used for the preparation of In$_2$Se$_3$ thin films, which include chemical bath deposition [19], spray pyrolysis [5], co-evaporation [20], electrodeposition [21], chemical vapor transport [22], hot injection method [23], sol–gel technique [24], molecular beam epitaxy (MBE) [25], radio frequency (RF) magnetron sputtering [26], and thermal evaporation [27]. Among these, RF sputtering is a prominent method due to its simplicity, scalability, and compatibility with large-area production.

In recent years, photodetectors have become essential components in various technological applications such as flame detection, defense applications, optical communication, target tracking, healthcare-related systems, missile warning systems, and so forth [28], [29], [30]. Developing efficient and high-performance photodetectors requires continuous research to improve their sensitivity, responsivity, and speed. One promising approach in this domain is the utilization of interdigital electrodes (IDE) in the design of photodetectors. These electrodes typically consist of finger-like structures arranged alternatingly, creating a periodic gap spacing between adjacent fingers [31]. These electrodes provide an effective means of enhancing the performance of photodetectors by enabling efficient charge collection and separation and facilitating the extraction of photo-generated carriers. MacKay et al. [32] reported that the biomolecules may be detected more precisely at a minimum IDE gap. Hase et al. [33] found that the use of IDEs enhances the performance of TiO$_2$ humidity sensors. Zhao et al. [34] observed that the gap between IDEs significantly affects the performance of a SnO$_2$-modified MoS$_2$ capacitive humidity sensor. They noted that a sensor with a minimum 5 $\mu$m gap exhibited the highest sensitivity (161 $\mu$F/% RH) at low humidity levels. In another study, Mathur et al. [35] observed the impact of IDE gap size on the biosensing of cardiac troponin-I. They reported a significant % sensitivity improvement of 50% when reducing the spacing from 75 to 5 $\mu$m. To optimize the performance of In$_2$Se$_3$ photodetectors, various device engineering strategies have been explored, including the design of IDE.

The IDEs are commonly used in photodetectors, specifically in devices such as metal-semiconductor-metal (MSM) photodetectors and finger photodiodes [36], [37]. The critical dimensions of IDEs can significantly affect the performance and characteristics of photodetectors. In particular, the gap spacing between the IDE fingers is crucial in determining the device's overall performance [38]. Controlling the size and spacing allows for manipulating the electric field distribution within the device's active region. It, in turn, influences the carrier transport properties, photoresponse, and, ultimately, the overall performance of the photodetector. By optimizing the IDE gap during the fabrication process, it is possible to enhance the device's performance and achieve superior photodetection capabilities. With this motivation, we studied the influence of the IDE gap on the performance of the In$_2$Se$_3$ photodetector. In this work, the $\gamma$-In$_2$Se$_3$ films were deposited on indium tin oxide (ITO)-coated IDEs using the RF sputtering method at optimized process parameters. The structural, morphological, and optical characteristics have been studied in light of their use as a photodetector. The high-quality, compact, and uniform $\gamma$-In$_2$Se$_3$ films were obtained using RF-magnetron sputtering. Finally, the photodetector properties of $\gamma$-In$_2$Se$_3$-based photodetectors were investigated for various IDE spacing, bias voltage, and light intensity.

## II. Experimental

### A. Fabrication of IDEs

The fabrication stages of ITO-coated IDEs are discussed in a previous work [26]. The IDE pattern was first printed on glossy paper using a LaserJet Pro M202 dw printer. Then, heat treatment transferred the pattern onto a cleaned ITO-coated glass substrate. Then, the IDE mask was coated on the ITO substrate. The Zn dust was spread over the substrate, and dilute HCl was added dropwise. The reaction between Zn dust and HCL, the uncovered ITO is etched out from the substrate. The covered ITO gives a conducting IDE finger pattern. The ITO-coated IDE substrate was then cleaned with acetone, isopropyl alcohol (IPA), and distilled water. The electrode length was 9 mm, and the width was 1.25 mm. The total area of the only electrode in the device is 67.5 mm$^2$ with three IDE pairs. The separation between the two electrodes was varied as 335, 440, 610, and 990 $\mu$m. Therefore, the total active area for 335, 440, 610, and 990 $\mu$m electrode gaps was 24.25, 29.5, 38, and 57 mm$^2$, respectively. The device's active area increased due to an increased electrode gap. In this study, the number of electrode pairs was kept the same (three electrode pairs with the same width for all devices).

### B. Deposition of $\gamma$-In$_2$Se$_3$ Films

The IDE substrates were ultrasonically cleaned for 15 min in acetone, IPA, and distilled water separately. After loading a clean substrate on the substrate holder, a base pressure $\sim 10^{-6}$ Torr was attained using rotary and turbomolecular pumps. A 4 inch target (99.99%) was used to deposit In$_2$Se$_3$ thin film. The target was pre-sputtered for 10 min to remove the oxide layer from the target surface. The optimized deposition parameters for these thin films are listed in Table I.

To improve the crystallinity and adhesion, post-deposition annealing of films was carried out for 60 min at 300 °C in a vacuum tubular furnace under a base pressure of $2 \times 10^{-2}$ mbar. Then, the naturally cooled films were used for the characterization. The thickness of the film was measured using a cross-sectional field emission scanning electron microscopy (FE-SEM) image and was found to be $\sim$200 nm.

| Process Parameter | Value |
|---|---|
| Deposition pressure | 5 Pa |
| Substrate temperature | 50 °C |
| Target to substrate distance | 7 cm |
| Deposition time | 15 min |
| RF power | 100 W |
| Annealing temperature | 300 °C |

## C. Material Characterization

The crystal structure of $In_2Se_3$ films was analyzed using an X-ray diffractometer (Bruker AXS; D8 Advance). The deposited film phase was confirmed by Raman spectroscopy (Renishaw InVia Raman microscopy). The surface morphology was investigated using Nova NanoSEM 450 FE-SEM. The elemental composition of prepared films was examined with an energy-dispersive spectrometer (Oxford Instruments, 51-ADD0058). The optical absorbance and transmittance measurements were performed using a UV-Visible-NIR spectrophotometer (JASCO, V-670). Thermo Scientific's K-Alpha+, U.K. Machine with a resolution of 0.1 eV was used for the X-ray photoelectron spectroscopy (XPS) spectra.

## III. RESULTS AND DISCUSSION

### A. Structural and Morphology Properties

Fig. 1 shows the structural and morphological properties of $\gamma$-$In_2Se_3$ thin film synthesized using RF-magnetron sputtering at optimized process parameters. Fig. 1(a) shows the X-ray diffraction (XRD) pattern for $In_2Se_3$ film prepared using the RF sputtering method and then annealed at 300 °C. The XRD pattern indicates that the diffraction peaks of $In_2Se_3$ can be well indexed to hexagonal crystal structure with $\gamma$-phase of $In_2Se_3$. All the diffraction peaks are matched well with JCPDS No. # 01-071-0250. The sharpness and intensity of XRD peaks indicate the high crystallinity of $\gamma$-$In_2Se_3$ thin films. The high crystallinity implies fewer grain boundaries and defects within the material. The grain boundaries act as trapping sites for carriers, reducing their mobility and increasing recombination losses. Therefore, the decrease in grain boundaries enhances the electrical conductivity and improves the performance of the photodetector [39]. No other impurity peaks were observed in the XRD pattern, which indicates the formation of high purity $\gamma$-$In_2Se_3$ thin film. As indicated by the XRD patterns, the absence of secondary phases or impurities ensures uniform electrical properties throughout the material. Any secondary phases could introduce localized states within the bandgap, acting as recombination centers for charge carriers, thus degrading the electrical performance of the device. The crystallite size associated with each crystal orientation was calculated using Debye Scherrer equation [26]. The crystallite size was found to be ~28, 24, 40, 38, 32, 30, and 34 nm for (101), (102), (110), (006), (116), (300), and (306) crystal planes, respectively.

Fig. 1(b) shows the Raman spectra of $In_2Se_3$ thin film. Two Raman active modes are observed at ~150 and ~248 cm$^{-1}$. These results are consistent with the earlier reported data,

confirming the formation of $\gamma$-phase [40], [41], [42]. The XPS is used to study the elemental and bond composition of $\gamma$-$In_2Se_3$, as shown in Fig. 1(c) and (d). The peaks observed at binding energies of ~443, ~451, and ~55 eV correspond to In 3d$_{5/2}$, In 3d$_{3/2}$, and Se 3d, respectively. Fig. 1(e) shows the morphology of $\gamma$-$In_2Se_3$ thin film. The FE-SEM images show the formation of dense, compact, and slightly spherical shape morphology of $In_2Se_3$ film. Fig. 1(f) shows the EDS spectra of $In_2Se_3$ film. The prepared $\gamma$-$In_2Se_3$ film shows an atomic % ratio of indium (In) to selenium (Se) ~2:3, which confirms the formation of stoichiometric $In_2Se_3$ films. These results confirm the formation of high-quality and pure $\gamma$-$In_2Se_3$ film by the RF magnetron sputtering.

### B. Optical Properties

Fig. 2(a) shows the UV-Visible absorption and transmission spectra of $In_2Se_3$ film synthesized by RF-magnetron sputtering at optimized process parameters. The absorption spectra reveal high absorbance within the UV-Visible wavelength range. The fringes observed in the transmittance spectra are due to the low surface roughness, low defect density, and high crystallinity [43] of $In_2Se_3$ film synthesized by RF-magnetron sputtering at optimized process parameters.

The coefficient of absorption ($\alpha$) can be calculated from the absorbance spectra by using the relation [44]

$$\alpha = 2.303 \times \frac{A}{t} \tag{1}$$

where $A$ is absorbance, and $t$ is the thickness of the film.

The optical bandgap of the prepared $\gamma$-$In_2Se_3$ films is estimated from the absorption coefficient using Tauc's formula [25]

$$(\alpha h\nu)^2 = A(h\nu - E_g) \tag{2}$$

where $h\nu$ is the incident photon energy, and $A$ is constant. Tauc's plot for bandgap calculation of $\gamma$-$In_2Se_3$ films is shown in Fig. 2(b). The bandgap of the $\gamma$-$In_2Se_3$ thin film was 1.98 eV.

### C. Photodetector Properties

The $\gamma$-$In_2Se_3$, with a direct bandgap of 1.98 eV, is a promising material for applications in optoelectronic devices, such as photodetectors. To investigate the photodetection performance of the optimized $\gamma$-$In_2Se_3$, photodetectors were fabricated on ITO-coated IDEs substrates with variable electrode spacing. The schematic of the fabricated photodetector and actual photograph is shown in Fig. 3.

Fig. 4 shows the SEM images of ITO-coated IDE substrates with different electrode spacing. The measured electrode spacing was 335, 440, 610, and 990 $\mu$m. First, we explored the photoresponse properties of the $\gamma$-$In_2Se_3$-based photodetectors fabricated on ITO-coated IDEs using $\gamma$-$In_2Se_3$ thin films obtained at optimized process parameters. For photoresponse measurements of $\gamma$-$In_2Se_3$ based photodetector, Keithley source meter (2450) was used.

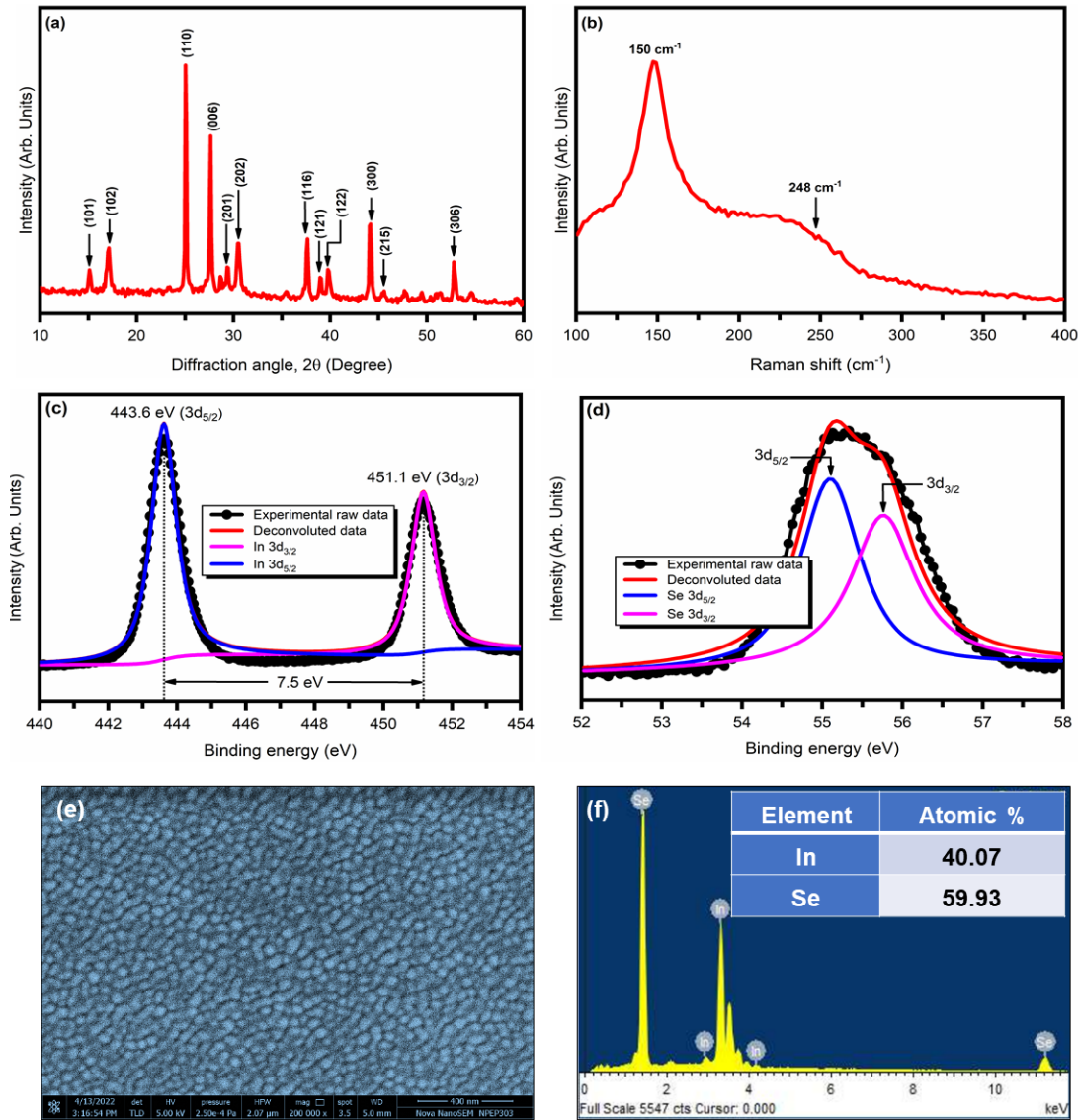Fig. 5(a) shows the full view of 440 $\mu$m electrode spacing measured using the FE-SEM. The thickness of the $In_2Se_3$ film

Fig. 1. (a) XRD pattern, (b) Raman spectra, (c) XPS spectra of-indium, (d) XPS spectra of selenium, (e) FE-SEM image, and (f) EDS spectra of $\gamma$-In$_2$Se$_3$ film deposited using RF-magnetron sputtering at optimized process parameters.

was measured using a cross-sectional FE-SEM image and was found to be $\sim$200 nm [Fig. 5(b)].

Fig. 6 shows the experimental setup used for the photoresponse measurements. The Class ABA Solar Simulator ORIEL Sol 2 A 94022 A was used for white light illumination with a 12 mW/cm$^2$ power density. The performance of photodetectors relies on three key factors: photoresponsivity, photodetectivity and photosensitivity. These three parameters are critical in determining the device's ability to detect and respond to incident light accurately. The photoresponsivity measures the electrical output generated by the photodetector in response to incident light power.

Photoresponsivity is typically expressed as the ratio of the generated photocurrent to the incident optical power. The photoresponsivity is determined using the relation [45], [46]

$$R_\lambda = \frac{\Delta I}{P_\lambda \times A} \tag{3}$$

where $A$ is the active area of the film, $\Delta I$ is the photocurrent generated by the photodetector, and $P_\lambda$ is the power density of incident light (12 mW/cm$^2$).

Photodetectivity ($D^*$) quantifies the ability of a photodetector to convert incident light power into an electrical signal and is calculated using the formula [46]

$$D^* = \frac{R_\lambda}{(2 \times e \times J_{\text{Dark}})^{\frac{1}{2}}} \tag{4}$$

where $J_{\text{Dark}}$ is the dark current density and $e$ is the electron charge.

The photosensitivity ($\xi$) is calculated using the formula [45]

$$\xi = \frac{I_{\text{Photo}} - I_{\text{Dark}}}{I_{\text{Dark}}}. \tag{5}$$

Fig. 7(a) displays the current–voltage ($I$–$V$) characteristics of $\gamma$-In$_2$Se$_3$ photodetectors fabricated at different IDE spacings. The $I$–$V$ characteristics were measured in a dark
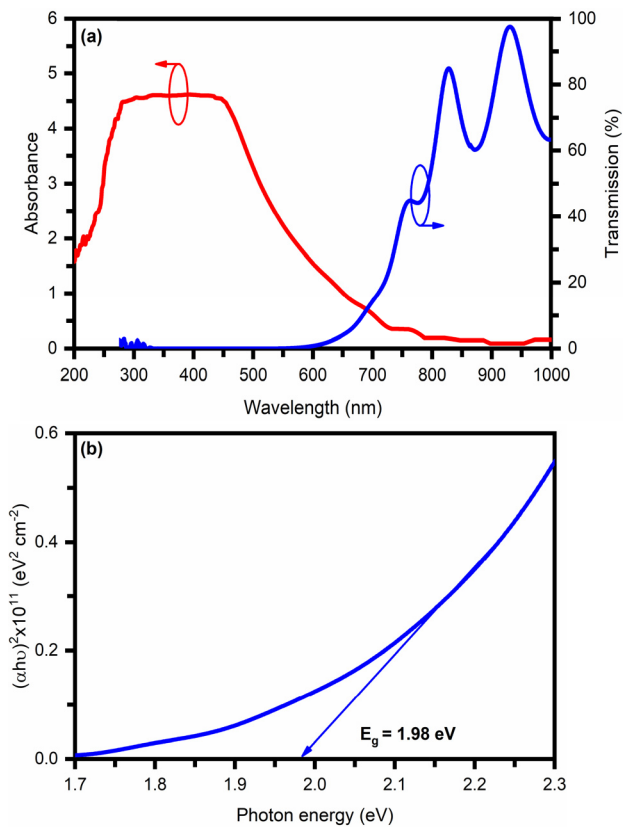
Fig. 2. (a) UV-Visible absorbance and transmission spectra and (b) Tauc plot for the band gap measurement of $\gamma$-In$_2$Se$_3$ film synthesized by RF-magnetron sputtering at optimized process parameters.
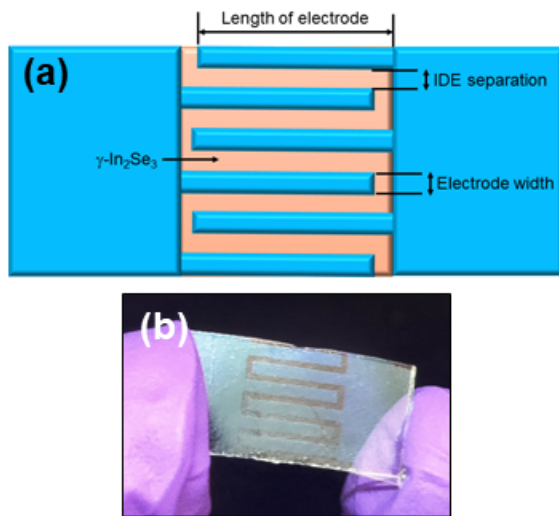


Fig. 3. (a) Schematic of ITO-coated interdigital electrodes (IDEs) and (b) actual photograph of $\gamma$-In$_2$Se$_3$-based photodetector fabricated on ITO-coated IDEs.



Fig. 4. Electrode spacing measured using the SEM images. (a) 335, (b) 440, (c) 610, and (d) 990 $\mu$m.



Fig. 5. (a) Full view of 440 $\mu$m electrode spacing measured using the SEM images. (b) Thickness measurement of In$_2$Se$_3$ film using cross-sectional FE-SEM.

chamber for light and dark conditions. The maximum photocurrent is observed at a minimum electrode spacing of 335 $\mu$m. As the interdigital spacing between electrodes increases, the photocurrent decreases due to increased electrode surface area; hence, the resistance increases. Fig. 7(b) illustrates the photoresponse of the $\gamma$-In$_2$Se$_3$ photodetector at a 0.5 V bias voltage. When a voltage is applied to the IDEs,
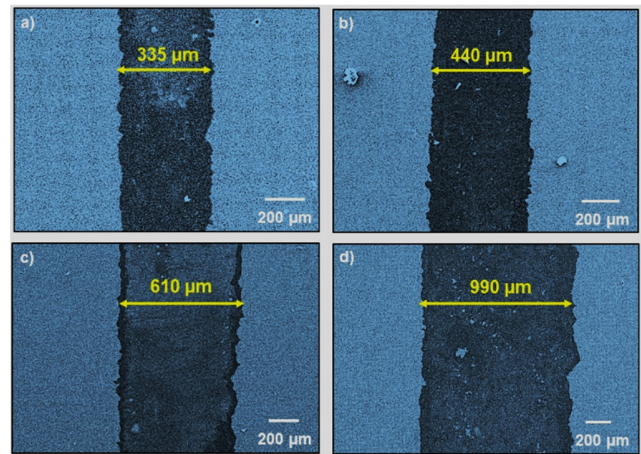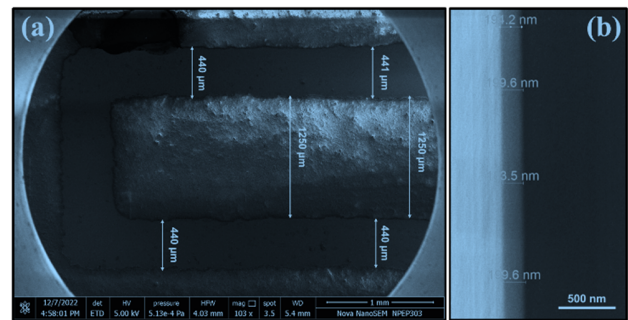
an electric field is generated between them. The strength of this electric field diminishes as the electrode spacing increases.

On the other hand, a smaller IDE spacing leads to a more concentrated electric field, assisting the efficient separation and collection of photogenerated charge carriers at the electrodes. It produces a higher photocurrent as more charge carriers contribute to the overall current. Moreover, a reduced IDE spacing minimizes carrier recombination, where charge carriers neutralize each other, thus enhancing device efficiency. The maximum photocurrent, observed at a 335 $\mu$m IDE spacing, reached 187 nA. However, the photocurrent diminishes notably with larger IDE spacing, yielding 147, 115, and 46 nA photocurrent for 440, 610, and 990 $\mu$m spacings, respectively. The spacing between the electrodes influences the distribution of the electric field within the photodetector. A smaller electrode spacing creates a stronger and more uniform electric field across the photodetector material. This enhanced field aids in efficiently separating photogenerated electron–hole pairs, thereby increasing the photocurrent. Conversely, larger electrode spacings result in weaker electric fields, which can lead to slower and less efficient charge carrier separation.

In Fig. 7(c), changes in photoresponsivity and detectivity are depicted based on IDE spacing. As the spacing increases, there is a noticeable decline in photocurrent, leading to a decrease in photoresponsivity from 14.83 to 2.58 $\mu$A/W. The increase in the electrode spacing typically enlarges the photoactive
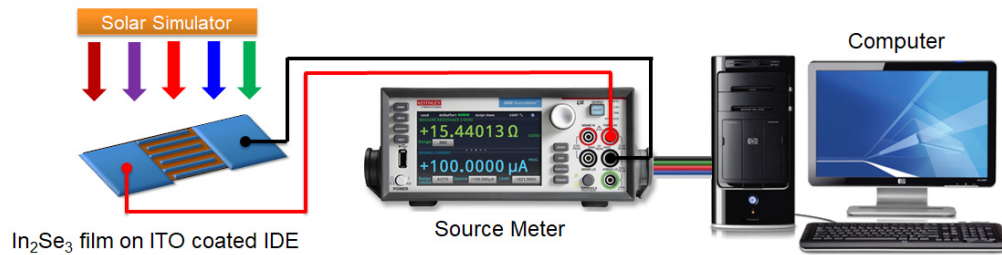
Fig. 6.  Schematic of photoresponse measurements of $\gamma$-In$_2$Se$_3$-based photodetectors.
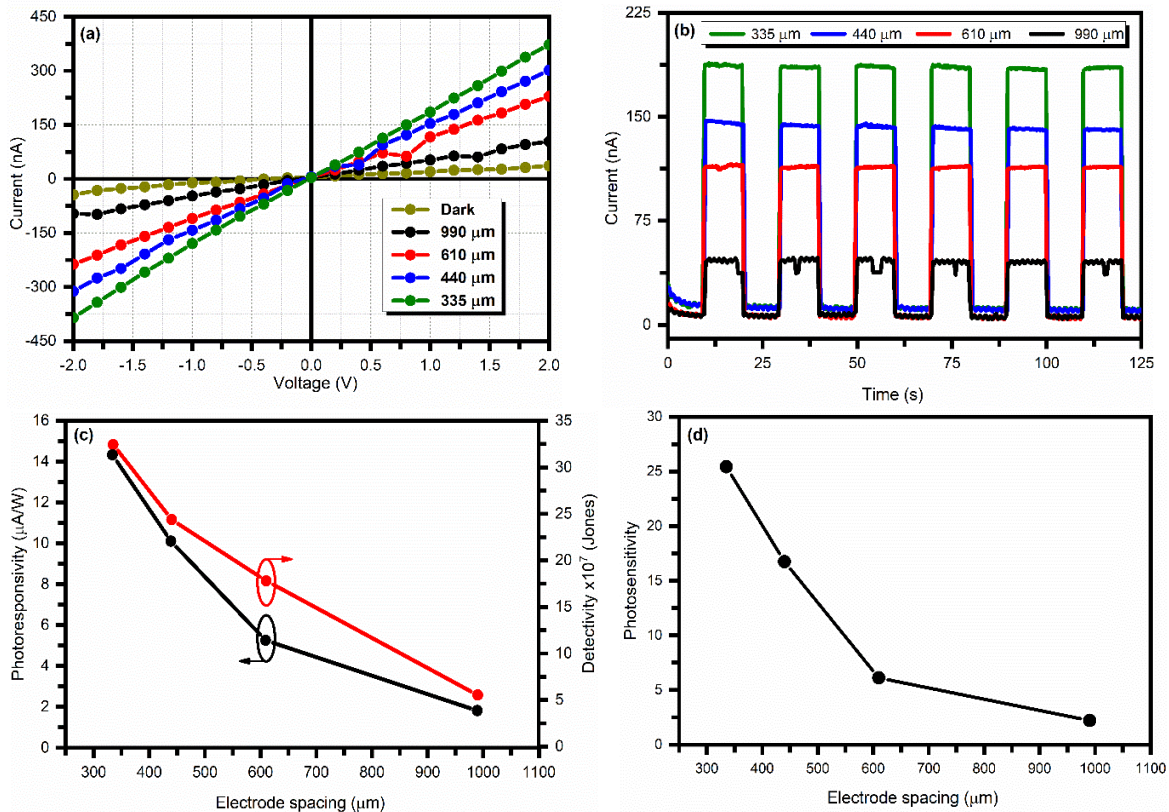


Fig. 7.    (a) $I$–$V$ characteristics. (b) Time-resolved photoresponse at a bias voltage of 0.5 V. (c) Photoresponsivity and photodetectivity. (d) Photosensitivity of $\gamma$-In$_2$Se$_3$-based photodetector at various interdigital electrode spacing.

area, allowing for greater light absorption. However, this can also lead to increased series resistance and potential recombination losses, which may negatively impact the overall photoresponsivity. Conversely, reducing the electrode spacing decreases the photoactive area but can enhance charge carrier collection efficiency and reduce recombination, potentially increasing the photoresponsivity of the device. Therefore, the photoresponsivity of the photodetector is enhanced with a decrease in electrode spacing or gap. Similarly, detectivity drops from $31.3 \times 10^7$ to $3.85 \times 10^7$ Jones as the IDE spacing increases from 335 to 990 $\mu$m. Fig. 7(d) represents the photosensitivity curve of the $\gamma$-In$_2$Se$_3$-based photodetector as a function of IDE spacing. The photosensitivity reduces from 25.42 to 2.21 with an increase in spacing from 335 to 990 $\mu$m.

The time-resolved photoresponse characteristics of In$_2$Se$_3$-based photodetector with variation in IDE spacing are shown in Fig. 8. The white light illumination source

was switched ON and OFF periodically at 10 s intervals. The bias voltage between the two electrodes was kept constant at 0.5 V. The photoresponse displayed three transient regimes in each curve: first, the sharp rise. The second is the steady state, and the third is the sharp decay. These results indicate that all $\gamma$-In$_2$Se$_3$-based photodetectors exhibited excellent photoresponse properties. The ON/OFF ratio is a critical parameter for assessing the performance of photoresponsive devices, indicating the contrast between the device's current under illumination (ON state) and in darkness (OFF state). We have measured the ON/OFF ratios for all devices with different electrode spacings. At room temperature under normal atmospheric conditions, the $\gamma$-In$_2$Se$_3$-based photodetector fabricated with a 335 $\mu$m electrode gap exhibited a dark current of ~12 nA, which increased to about ~185 nA under white light irradiation, resulting in an ON/OFF ratio of 15.41. For a 440 $\mu$m IDE spacing, the
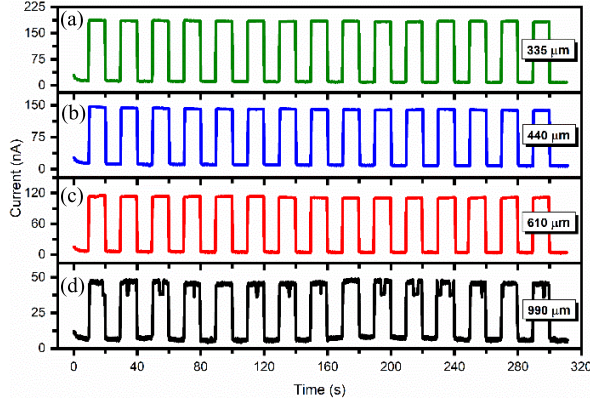
Fig. 8. Time-resolved photoresponse of $\gamma$-In$_2$Se$_3$-based photodetectors fabricated at various interdigital electrode spacing (a) 335, (b) 440, (c) 610, and (d) 990 $\mu$m.

dark current was around 11 nA, and the photocurrent reached approximately 142 nA under white light illumination, yielding an ON/OFF ratio of 12.90. With further increase in electrode spacing from 610 to 990 $\mu$m resulted in dark currents of $\sim$10 and $\sim$6 nA and photocurrents of $\sim$114 and $\sim$46 nA, with ON/OFF ratios of 11.40 and 7.66, respectively. These results highlight the dependency of photoresponse performance on electrode spacing in $\gamma$-In$_2$Se$_3$-based photodetectors. The dark current, which is the current that flows through the photodetector in the absence of illumination, is influenced by the electrode spacing. Larger spacings tend to reduce the dark current because the longer path and weaker electric field make it harder for thermally generated carriers to reach the electrodes. On the other hand, smaller spacings can increase the dark current due to the stronger electric field and shorter paths facilitating carrier movement. The $\gamma$-In$_2$Se$_3$-based photodetectors exhibit stable photoresponse across different IDE spacings. The photoresponse maintains an exact square wave nature up to an IDE spacing of 610 $\mu$m. However, this square wave characteristic is disturbed when the interelectrode spacing is increased to 990 $\mu$m.

The performance of the $\gamma$-In$_2$Se$_3$ photodetector was further explored by calculating the rise time and decay time. The rise time ($\tau_{rise}$) is defined as the time required for a photodetector to reach 90% of its maximum photocurrent value from its dark current value. Similarly, the decay time ($\tau_{decay}$) is defined as the time required for the photodetector to reach 10% of its minimum dark current value from its photocurrent value [26]. The rise and decay processes follow an exponential law [47], [48], [49]:

$$I = I_0\left(1 - e^{\frac{-t}{\tau_{rise}}}\right) \tag{6}$$

$$I = I_0 e^{\frac{-t}{\tau_{decay}}} \tag{7}$$

where $I_0$ is the photocurrent, $\tau_{rise}$ and $\tau_{decay}$ are the rise and decay times, respectively, and $t$ is the time constant.

Fig. 9 shows a single-cycle photoresponse of $\gamma$-In$_2$Se$_3$-based photodetectors at various IDE spacing to measure rise and decay time. As seen, the In$_2$Se$_3$ films deposited on a 335 $\mu$m electrode gap give a fast response to light with a rise time of $\sim$99 ms and a decay time of $\sim$61 ms. But, as the

gap size increases to 990 $\mu$m, the rise time increases to 222 ms and the decay time to 138 ms. With smaller electrode spacing, the carriers have a shorter distance to travel, reducing their transit time. This leads to a faster response time and higher photocurrent because the carriers are collected more quickly before recombining them. In larger spacings, the increased distance results in longer transit times, which can reduce the overall photocurrent due to higher chances of recombination before collection. It can be seen that the rise and decay time are both influenced by IDE spacing. The response time is expressed as [50] and [51]

$$\tau = \sqrt{\tau_{tr}^2 + (RC)^2} \tag{8}$$

where, $\tau_{tr}^2$ is transit time, $R$ and $C$ are the detector's loaded and series resistance and internal capacitance. The response time $\tau$ can be limited either by the $RC$ time constant or by the carrier transit time. For devices with large electrode spacing and low electric field, the transit time usually determines their response time. Conversely, the $RC$ time constant limits the response time when the electrode spacing is small enough. In this study, the device capacitance is calculated by [50], [51]

$$C = \frac{A\epsilon_0\left(\epsilon_{In_2Se_3} + 1\right)^2}{L + W} \frac{\pi}{4\ln\left(\left(\frac{8}{\pi}\right) + \left(\frac{L}{W}\right)\right)} \tag{9}$$

where $\varepsilon_{In_2Se_3}$ and $\varepsilon_0$ are the dielectric constant of $\gamma$-In$_2$Se$_3$ and the vacuum permittivity, respectively. $L$ is the interdigital spacing, $A$ is the photodetector area, and $W$ is the finger width (1.25 mm). The estimated capacitance values for the fabricated photodetector devices are $\sim$39, 35.7, 30.3, and 22.3 pF, corresponding to IDE spacings of 335, 440, 610, and 990 $\mu$m, respectively. These capacitance values are considered small, eliminating the possibility of determining the response time using the $RC$ limit. Instead, the response time may be influenced by the transit time limit. The transit time ($\tau_{tr}$) can be expressed as [52], [53]

$$\tau_{tr} = \frac{L^2}{V\mu_n} \tag{10}$$

where $\mu_n$ is the electron mobility of $\gamma$-In$_2$Se$_3$, and $V$ is applied bias.

In low electric field conditions, since $\mu_n$ and $V$ are constants, the transit time proportional to the square of the length ($L$). Consequently, decreasing the IDE spacing reduces the transit time. Thus, the transit time is directly proportional to the interdigital spacing. Therefore, minimizing the interdigital spacing reduces the response time of the $\gamma$-In$_2$Se$_3$ photodetector. Table II provides the rise and decay time values at various IDE spacings.

As seen, the $\gamma$-In$_2$Se$_3$-based photodetector fabricated at IDE spacing of 335 $\mu$m showed excellent photodetector properties, having the highest photoresponsivity and detectivity of 14.8 $\mu$A/W and 31.3 $\times$ 10$^7$ Jones, respectively, with a fast rise time of 99 ms and decay time of 61 ms.

After optimizing the IDE spacing, we have systematically varied the applied bias voltage of the photodetector. Fig. 10 shows the photodetector properties of $\gamma$-In$_2$Se$_3$-based photodetector with a 335 $\mu$m IDE spacing, characterized under
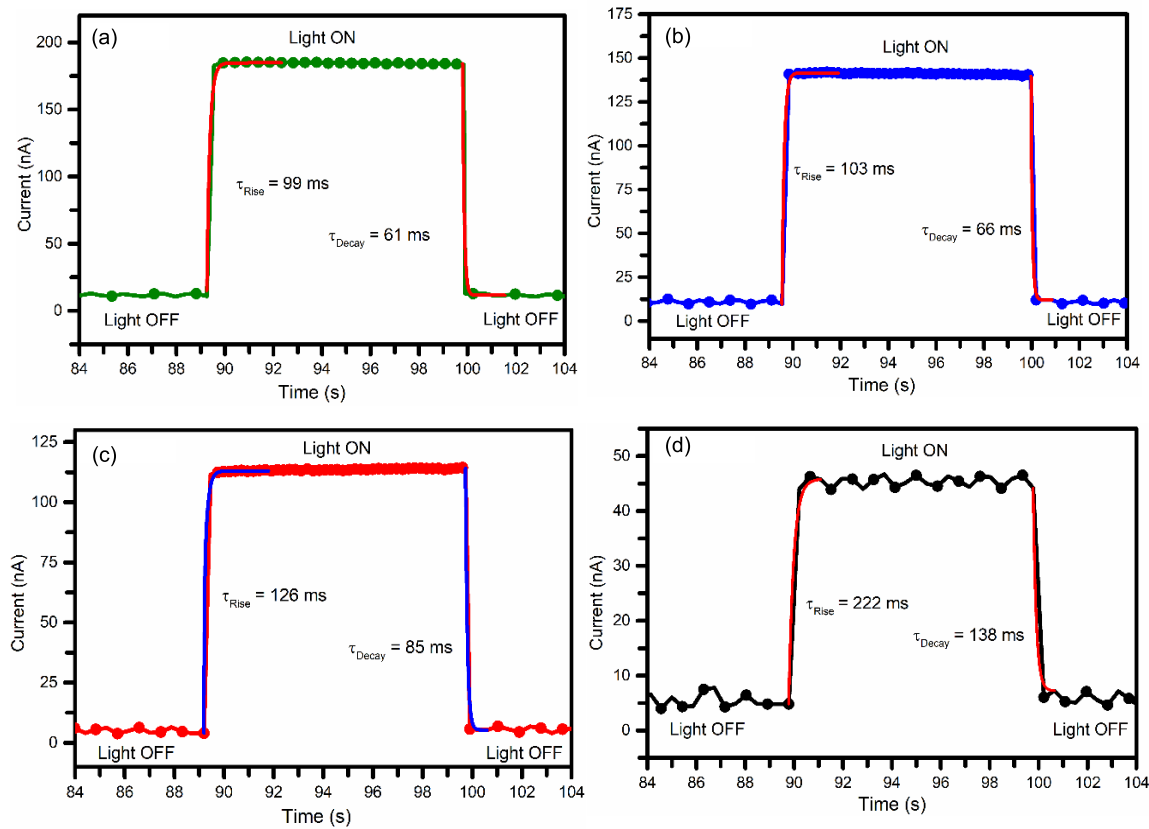
Fig. 9. Single cycle photoresponse of $\gamma$-In$_2$Se$_3$-based photodetector at various electrode spacing (a) 335, (b) 440, (c) 610, and (d) 990 $\mu m$.

TABLE II
PHOTORESPONSIVITY, PHOTOSENSITIVITY, DETECTIVITY, RISE, AND DECAY TIME FOR PHOTODETECTOR BASED ON In$_2$Se$_3$ FILMS SYNTHESIZED AT VARIOUS ELECTRODE GAP (WHITE LIGHT ILLUMINATION, LIGHT INTENSITY = 27 mW/cm$^2$, BIAS VOLTAGE = 0.5 V)

| Electrode spacing (μm) | Photoactive area (mm$^2$) | Photo-responsivity R$_\lambda$ (μA/W) | Photo-sensitivity (ξ) | Photodetectivity (D*) x 10$^7$ Jones | Rise time $\tau_{Rise}$ (ms) | Decay time $\tau_{Decay}$ (ms) |
|---|---|---|---|---|---|---|
| 335 | 24.25 | 14.8 | 09.4 | 31.3 | 99 | 61 |
| 440 | 29.5 | 11.1 | 14.6 | 22.1 | 103 | 66 |
| 610 | 38 | 08.1 | 39.3 | 11.4 | 126 | 85 |
| 990 | 57 | 02.5 | 45.3 | 3.85 | 222 | 138 |

different bias potentials. Fig. 10(a) shows that the photocurrent exhibits a linear relationship with rising bias potentials. The applied bias potential generates an electric field between the electrodes, and as this bias potential increases, the electric field intensity also increases. Upon illumination, electron–hole pairs are generated and are subsequently attracted toward the electrodes due to the electric field. The increased bias potential enhances the electric field strength, providing an increased driving force for the carriers. It enables the carriers to move more rapidly toward the electrodes, contributing to the observed linear increase in photocurrent with an increase in bias potential. In Fig. 10(b), a linear increase is observed in both photocurrent and dark current, indicating the formation of ohmic contact between the electrodes and the $\gamma$-In$_2$Se$_3$ film. Notably, the rate of increase in photocurrent surpasses that of dark current as the bias potential increases. Consequently,

in Fig. 10(c), photoresponsivity and detectivity increase with an increase in bias potential. Fig. 10(d) reveals that photosensitivity remains constant despite the increasing bias potential due to consistent photo and dark current increments.

The Schottky barrier height (SBH) at the ITO/In$_2$Se$_3$ interface significantly influences the performance of the In$_2$Se$_3$ photodetector, particularly under different electrode spacing conditions. At zero bias, the SBH remains high (Fig. 11). Therefore, no current will pass through or be generated by the In$_2$Se$_3$ photodetector device in any direction as the net built-in electric field equals zero. That is, no external electric field drives the separation of charge carriers. Under illumination, the light excites (generates) electron–hole pairs while the Schottky barriers are still high, and no biasing voltage can overcome the barrier potentials. Although carrier concentration increases dramatically due to photoexcitation, the net photocurrent at
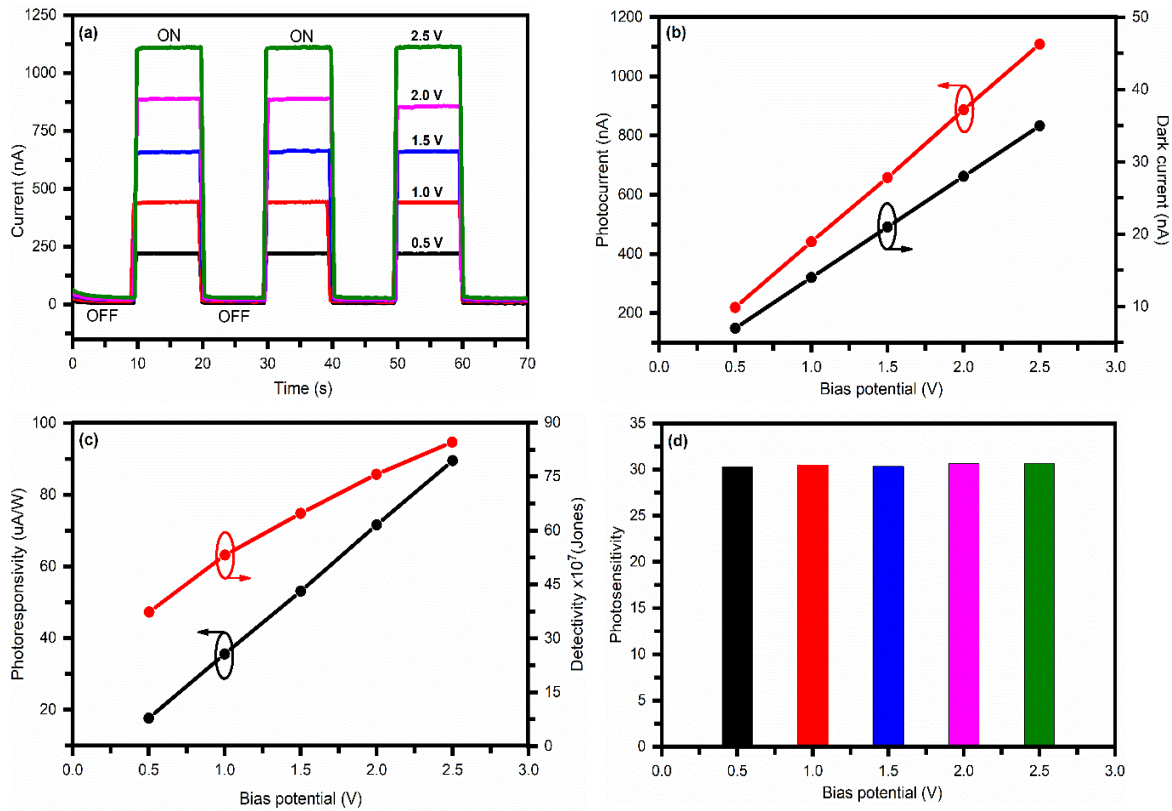
Fig. 10. (a) Photoresponse, (b) photocurrent and dark current, (c) photoresponsivity and photodetectivity, and (d) photosensitivity of $\gamma$-In$_2$Se$_3$-based photodetector fabricated optimized interdigital electrode spacing of 335 $\mu$m at various bias potentials.

zero voltage is also zero as the carriers are trapped between the two electrodes, and there is no possible path to collect them [54], [55]. The electrode spacing does not significantly influence the barrier height at zero bias. The Schottky barriers will be lowered at low biasing voltage, improving carrier injection slightly. The low bias voltage creates a weak electric field across the two electrodes. This field assists in separating and transporting photogenerated carriers (electrons and holes), thereby increasing the photocurrent compared to zero bias. The dark current also begins to rise slightly with the applied bias due to the enhanced drift of thermally generated carriers. At high bias voltages, the electric field becomes significant enough to substantially lower the SBH, especially with smaller electrode spacings, which promotes increased carrier injection and higher photocurrent. This effect is augmented by potential tunneling phenomena under high electric fields, further boosting photocurrent. Conversely, larger electrode spacings exhibit less pronounced reductions in SBH and consequently lower photocurrents [54], [55].

It's crucial to emphasize that the photoresponse of a photodetector is significantly affected by the intensity of incident radiation. In this study, we varied the intensity of incident light by adjusting the input power of the solar simulator. Fig. 12 shows the photoresponse properties of $\gamma$-In$_2$Se$_3$-based photodetectors fabricated at optimized IDE spacing of 335 $\mu$m and bias potential of 0.5 V at different incident radiation intensities. Fig. 12(a) illustrates the relationship between photocurrent and light intensity. As light intensity
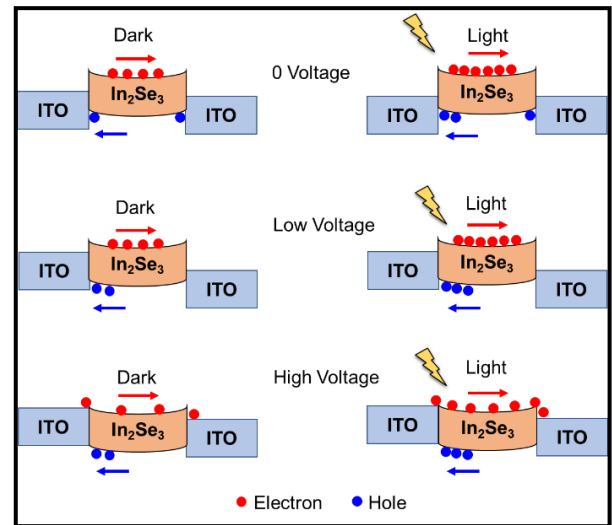


Fig. 11. Schematics of the conduction mechanism of In$_2$Se$_3$ photodetector under dark and white light illumination at different bias voltage.

rises, the increased photon density boosts the number of charge carriers, resulting in a linear increase in photocurrent. The increased light intensity leads to more photons striking the photodetector's surface area per unit time, increasing photon absorption and electron–hole pair generation. The greater number of excited electrons translates to increased current flow, causing a rise in photocurrent. In Fig. 12(b), photosensitivity
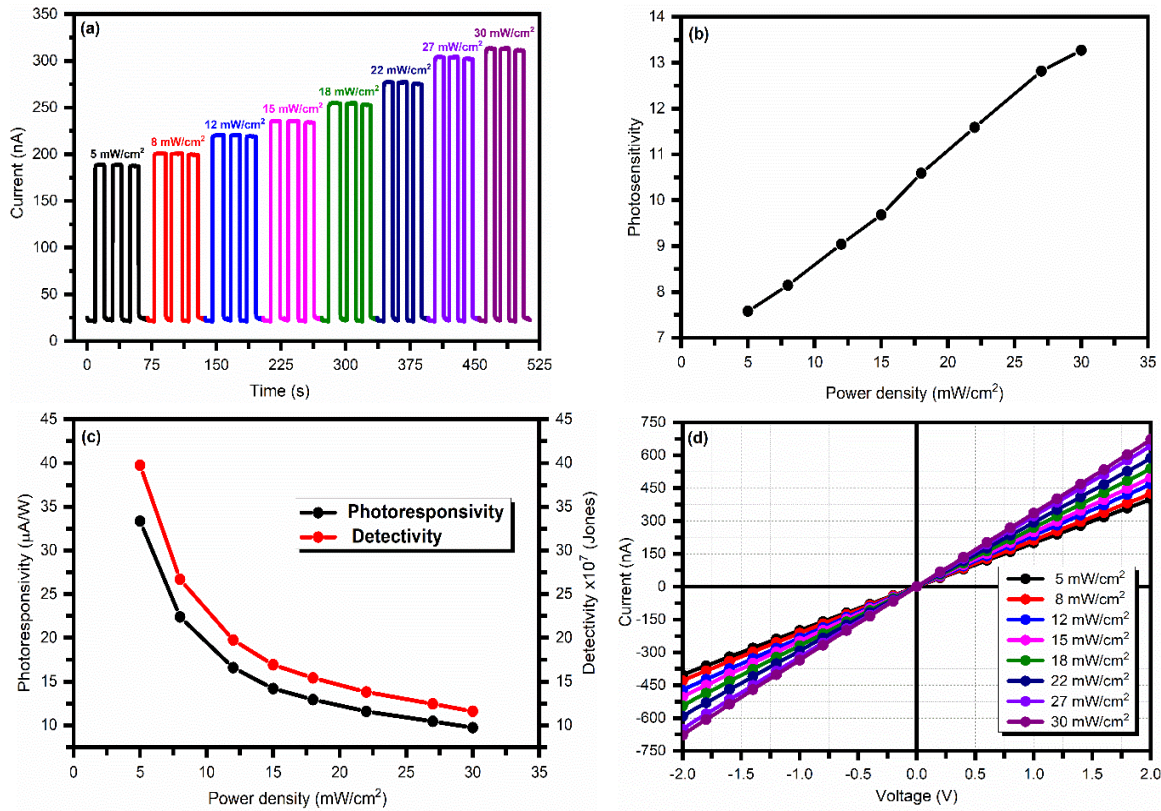
Fig. 12. (a) Time-resolved photoresponse at a bias voltage of 0.5 V. (b) Photosensitivity. (c) Photoresponsivity and photodetectivity. (d) *I–V* characteristics of $\gamma$-In$_2$Se$_3$-based photodetector fabricated at optimized interdigital electrode spacing of 335 $\mu$m at various power densities of light.

is depicted as a function of incident light power density. The rise in photocurrent with increasing light intensity enhances photosensitivity. Photosensitivity increases from 7.6 to 13.3 as light intensity goes from 5 to 30 mW/cm$^2$. Fig. 12(c) displays photoresponsivity and detectivity as a function of light intensity. Both are inversely proportional to incident light power. Despite the rise in photocurrent with increased light intensity, there is a decrease in both photoresponsivity and detectivity due to higher power density. Photoresponsivity decreases from 33.36 to 9.73 $\mu$A/W, and detectivity falls from 3.97 $\times$ 10$^8$ to 1.16 $\times$ 10$^8$ Jones as light intensity goes from 5 to 30 mW/cm$^2$. Fig. 12(d) shows the IV characteristics of $\gamma$-In$_2$Se$_3$-based photodetectors as a function of light intensity. The linear increase in photocurrent with increased light intensity indicates ohmic contact formation.

The experimental data of photocurrent and power density of light fit with power law [30], [56]

$$I_{\text{photo}} = A P^\theta \qquad (11)$$

where $A$ is the proportionality constant, $P$ is the power of incident light, and $\theta$ determines the photocurrent response concerning the optical power density of incident light.

The $I_{\text{photo}}$ exhibited an intensity dependence of $\theta \sim 0.99$, as shown in Fig. 13, indicating an effective generation of charge carriers from photons. The value of $\theta$ which is close to unity reflects that the carrier trap states between the fermi level and the conduction band edge are very low [56], [57].
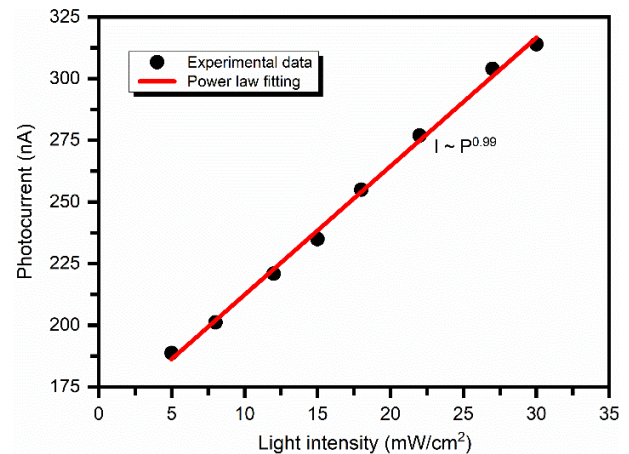


Fig. 13. Relationship between measured photocurrent and light intensity for $\gamma$-In$_2$Se$_3$ based photodetector.

The comparative analysis of the fabricated $\gamma$-In$_2$Se$_3$-based photodetectors with metal chalcogenide-based photodetectors fabricated using various methods presented in Table III provides a comprehensive understanding of these photodetectors' relative performance and efficiency. The performance of the fabricated $\gamma$-In$_2$Se$_3$-based photodetectors, particularly in terms of rise and decay times, is compared with previously reported IDE-based photodetectors presented in Table IV. The $\gamma$-In$_2$Se$_3$ shows better photoresponsivity, photosensitivity, fast rise, and decay time.

TABLE III
COMPARATIVE ANALYSIS OF THE RISE TIME AND DECAY TIME OF THE $\gamma$-In$_2$Se$_3$ BASED PHOTODETECTORS WITH
REPORTED EARLIER METAL CHALCOGENIDE PHOTODETECTORS

| Photoactive Material | Synthesis method | Rise time (s) | Decay time (s) | Ref. |
|---|---|---|---|---|
| SnS | Co-evaporation Technique | 1.2 | 3 | [58] |
| PbBi$_2$Se$_4$ | Solvothermal | 121 | 123 | [46] |
| WS$_2$ | PLD | 4.1 | 4.4 | [59] |
| MoS$_2$ | CVD | 20 | 1.23 | [60] |
| SnS | Thermal Evaporation | 2.4 | 2.7 | [61] |
| WS$_2$ | HWCVD | 51 | 88 | [62] |
| In$_2$Se$_3$ | Mechanical Exfoliation | 3.4 | 11 | [63] |
| In$_2$Se$_3$ | Mechanically Exfoliation Method | 3.87 | 4.35 | [64] |
| In$_2$Se$_3$ | Chemical Vapor Transport (CVT) | 0.6 | 4.1 | [9] |
| **In$_2$Se$_3$** | **RF sputtering** | **0.09** | **0.06** | **Present work** |

TABLE IV
COMPARATIVE ANALYSIS OF THE RISE TIME AND DECAY TIME OF INTERDIGITAL ELECTRODE BASED
PHOTODETECTORS WITH EARLIER REPORTED PHOTODETECTORS

| Photoactive Material | IDE gap ($\mu$m) | Synthesis method | Rise time (s) | Decay time (s) | Ref. |
|---|---|---|---|---|---|
| ZnO | 2 | Hydrothermal method | 3.8 | 2.6 | [65] |
| GaN | 800 | Plasma-assisted molecular beam epitaxy (PAMBE) | 121 | 123 | [66] |
| TiS$_2$ | 5 | Chemical vapor transport (CVT) | 0.3 | 0.18 | [67] |
| MoS$_2$ | -- | Exfoliation Method | 0.25 | 0.18 | [68] |
| CdS | 200 | RF sputtering method | 0.12 | 0.24 | [69] |
| P3HT | 10 | Spin-coating method | 35 | 48 | [70] |
| **In$_2$Se$_3$** | **RF sputtering** | **RF sputtering** | **0.09** | **0.06** | **Present work** |

## IV. CONCLUSION

In this study, $\gamma$-In$_2$Se$_3$ thin films were successfully deposited on IDE substrates using an RF-magnetron sputtering method at optimized process parameters. The formation of high-quality $\gamma$-In$_2$Se$_3$ was confirmed using XRD, Raman spectroscopy, XPS, FE-SEM, and energy dispersive spectroscopy (EDS) analyses. The XRD and Raman spectroscopy analysis shows that the prepared film has $\gamma$-phase with hexagonal crystal structure. The optical bandgap of $\gamma$-In$_2$Se$_3$ film was 1.98 eV. The FE-SEM analysis shows compact, dense, and pore-free $\gamma$-In$_2$Se$_3$ thin film formation. The EDS spectra confirm the formation of a stoichiometric $\gamma$-In$_2$Se$_3$ thin film. Furthermore, $\gamma$-In$_2$Se$_3$-based photodetectors were fabricated on ITO-coated IDEs at optimized process parameters. The influence of IDE spacing, bias voltage, and light intensity on photodetector properties was investigated in detail. The $\gamma$-In$_2$Se$_3$-based photodetector fabricated at IDE spacing of 335 $\mu$m showed excellent photodetector properties, having the highest photo-responsivity and detectivity of 14.8 $\mu$A/W and 31.3 $\times$ 10$^7$ Jones, respectively, with a fast rise time of 99 ms and decay time of 61 ms. In bias voltage variation, the $\gamma$-In$_2$Se$_3$-based photodetectors show a linear relationship between the change in current and the bias potential, suggesting the formation of ohmic contact between the $\gamma$-In$_2$Se$_3$ and ITO electrodes. In studying light intensity photoresponse, we varied the power density of light from 5 to 30 mW/cm$^2$ to investigate its impact on $\gamma$-In$_2$Se$_3$-based photodetectors. We observed a direct propor-

tionality between the generated photocurrent and the intensity of the incident light. However, at higher light intensities, we noted a decrease in photodetectivity from 3.97 $\times$ 10$^8$ to 1.16 $\times$ 10$^8$ Jones and a reduction in photoresponsivity from 33.36 to 9.73 $\mu$A/W for the $\gamma$-In$_2$Se$_3$-based photodetectors. In conclusion, the photodetector properties of $\gamma$-In$_2$Se$_3$-based photodetectors critically depend on IDE spacing, bias voltage, and light intensity.

## REFERENCES

[1] J. Wang, H. Yu, C. Hou, and J. Zhang, "Solution-processable 2D $\alpha$-In$_2$Se$_3$ as an efficient hole transport layer for high-performance and stable polymer solar cells," *Sol. RRL*, vol. 4, no. 3, Mar. 2020, Art. no. 1900428, doi: 10.1002/solr.201900428.

[2] C. Jeengar, M. Tomar, K. Jindal, A. Sharma, and P. K. Jha, "Influence of post deposition annealing on thermoelectric properties of In$_2$Se$_3$ thin films," *Mater. Sci. Semiconductor Process.*, vol. 153, Jan. 2023, Art. no. 107127, doi: 10.1016/j.mssp.2022.107127.

[3] G. D'Olimpio et al., "Solution-processed In$_2$Se$_3$ nanosheets for ultrasensitive and highly selective NO$_2$ gas sensors," *J. Mater. Chem. A*, vol. 11, no. 23, pp. 12315–12327, 2023, doi: 10.1039/d3ta01390a.

[4] X. Wang, Z. Feng, J. Cai, H. Tong, and X. Miao, "All-van der Waals stacking ferroelectric field-effect transistor based on In$_2$Se$_3$ for high-density memory," *Sci. China Inf. Sci.*, vol. 66, no. 8, Aug. 2023, Art. no. 182401, doi: 10.1007/s11432-022-3617-2.

[5] A. A. Yadav and S. D. Salunke, "Photoelectrochemical properties of In$_2$Se$_3$ thin films: Effect of substrate temperature," *J. Alloys Compounds*, vol. 640, pp. 534–539, Aug. 2015, doi: 10.1016/j.jallcom.2015.04.041.

[6] S. R. Mishra, V. Gadore, G. Yadav, and M. Ahmaruzzaman, "Next-generation energy storage: In$_2$S$_3$-based materials as high-performance electrodes for alkali-ion batteries," *Next Energy*, vol. 2, Jan. 2024, Art. no. 100071, doi: 10.1016/j.nxener.2023.100071.

[7] W. Zhang, Q. Su, B. Zhang, J. Peng, and Y. Li, "$\alpha$-In$_2$Se$_3$ nanostructure-based photodetectors for tunable and broadband response," *ACS Appl. Nano Mater.*, vol. 6, no. 10, pp. 8795–8803, May 2023, doi: 10.1021/acsanm.3c01190.

[8] K. Li, K. Ling, W. Li, and X. Liu, "Investigation of In$_2$Se$_x$O$_y$/In$_2$Se$_3$/Si dual-junction photodiode for self-powered broadband photodetection," *Appl. Phys. Lett.*, vol. 124, no. 3, Jan. 2024, Art. no. 031105, doi: 10.1063/5.0188557.

[9] M. Anandan et al., "High-responsivity broad-band sensing and photo-conduction mechanism in direct-gap $\alpha$-In$_2$Se$_3$ nanosheet photodetectors," *Nanotechnology*, vol. 31, no. 46, Nov. 2020, Art. no. 465201, doi: 10.1088/1361-6528/abac7e.

[10] W. Feng et al., "High-performance and flexible photodetectors based on chemical vapor deposition grown two-dimensional In$_2$Se$_3$ nanosheets," *Nanotechnology*, vol. 29, no. 44, Nov. 2018, Art. no. 445205, doi: 10.1088/1361-6528/aadc73.

[11] B. Wang, S. P. Zhong, Z. B. Zhang, Z. Q. Zheng, Y. P. Zhang, and H. Zhang, "Broadband photodetectors based on 2D group IVA metal chalcogenides semiconductors," *Appl. Mater. Today*, vol. 15, pp. 115–138, Jun. 2019, doi: 10.1016/j.apmt.2018.12.010.

[12] J. Yao, Z. Zheng, and G. Yang, "All-layered 2D optoelectronics: A high-performance UV–vis–NIR broadband SnSe photodetector with Bi$_2$Te$_3$ topological insulator electrodes," *Adv. Funct. Mater.*, vol. 27, no. 33, Sep. 2017, Art. no. 1701823, doi: 10.1002/adfm.201701823.

[13] J. Quereda, R. Biele, G. Rubio-Bollinger, N. Agraït, R. D'Agosta, and A. Castellanos-Gomez, "Strong quantum confinement effect in the optical properties of ultrathin $\alpha$-In$_2$Se$_3$," *Adv. Opt. Mater.*, vol. 4, no. 12, pp. 1939–1943, Dec. 2016, doi: 10.1002/adom.201600365.

[14] H. Cai, Y. Gu, Y.-C. Lin, Y. Yu, D. B. Geohegan, and K. Xiao, "Synthesis and emerging properties of 2D layered III–VI metal chalcogenides," *Appl. Phys. Rev.*, vol. 6, no. 4, Dec. 2019, Art. no. 041312, doi: 10.1063/1.5123487.

[15] P. D. Matthews, P. D. McNaughter, D. J. Lewis, and P. O'Brien, "Shining a light on transition metal chalcogenides for sustainable photovoltaics," *Chem. Sci.*, vol. 8, no. 6, pp. 4177–4187, 2017, doi: 10.1039/c7sc00642j.

[16] A. Waghmare et al., "Preparation and characterization of $\alpha$-In$_2$Se$_3$ thin-film photoanodes for photoelectrochemical water splitting," *J. Solid State Electrochemistry*, vol. 26, no. 1, pp. 219–232, Jan. 2022, doi: 10.1007/s10008-021-05054-1.

[17] C.-H. Ho and Y.-C. Chen, "Thickness-tunable band gap modulation in $\alpha$-In$_2$Se$_3$," *RSC Adv.*, vol. 3, no. 47, p. 24896, 2013, doi: 10.1039/c3ra44624g.

[18] R. B. Jacobs-Gedrim et al., "Extraordinary photoresponse in two-dimensional In$_2$Se$_3$ nanosheets," *ACS Nano*, vol. 8, no. 1, pp. 514–521, Jan. 2014, doi: 10.1021/nn405037s.

[19] P. P. Hankare, M. R. Asabe, P. A. Chate, and K. C. Rathod, "Structural, optical and microscopic properties of chemically deposited In$_2$Se$_3$ thin films," *J. Mater. Sci., Mater. Electron.*, vol. 19, no. 12, pp. 1252–1257, Dec. 2008, doi: 10.1007/s10854-008-9585-5.

[20] B. Thomas and T. R. N. Kutty, "Formation of single-phase indium selenide thin films by elemental evaporation," *Phys. Status Solidi (A)*, vol. 119, no. 1, pp. 127–138, May 1990, doi: 10.1002/pssa.2211190115.

[21] O. Dilmi and M. Benaicha, "Electrochemical synthesis of In$_2$Se$_3$ thin films from citrate Bath. Structural, optical and morphological investigations," *Russian J. Electrochemistry*, vol. 57, no. 5, pp. 462–470, May 2021, doi: 10.1134/s1023193521050049.

[22] C.-H. Ho, M.-H. Lin, and C.-C. Pan, "Optical-memory switching and oxygen detection based on the CVT grown $\gamma$- and $\alpha$-phase In$_2$Se$_3$," *Sens. Actuators B, Chem.*, vol. 209, pp. 811–819, Mar. 2015, doi: 10.1016/j.snb.2014.12.036.

[23] Y. Jiang et al., "Construction of In$_2$Se$_3$/MoS$_2$ heterojunction as photoanode toward efficient photoelectrochemical water splitting," *Chem. Eng. J.*, vol. 358, pp. 752–758, Feb. 2019, doi: 10.1016/j.cej.2018.10.088.

[24] I. H. Mutlu, M. Z. Zarbaliyev, and F. Aslan, "Indium selenide thin film preparation by sol–gel technique," *J. Sol-Gel Sci. Technol.*, vol. 43, no. 2, pp. 223–226, Jul. 2007, doi: 10.1007/s10971-007-1573-3.

[25] T. Okamoto, A. Yamada, and M. Konagai, "Growth and characterization of In$_2$Se$_3$ epitaxial films by molecular beam epitaxy," *J. Cryst. Growth*, vols. 175–176, pp. 1045–1050, May 1997, doi: 10.1016/s0022-0248(96)00984-0.

[26] Y. Hase et al., "Annealing temperature effect on structural and opto-electronic properties of $\alpha$-In$_2$Se$_3$ thin films towards highly stable photodetector applications," *J. Mol. Struct.*, vol. 1265, Oct. 2022, Art. no. 133336, doi: 10.1016/j.molstruc.2022.133336.

[27] R. Panda, R. Naik, and N. C. Mishra, "Low-temperature growth of $\gamma$ phase in thermally deposited In$_2$Se$_3$ thin films," *Phase Transitions*, vol. 91, no. 8, pp. 862–871, Aug. 2018, doi: 10.1080/01411594.2018.1508680.

[28] L. Singh, R. Singh, B. Zhang, S. Cheng, B. K. Kaushik, and S. Kumar, "LSPR based uric acid sensor using graphene oxide and gold nanoparticles functionalized tapered fiber," *Opt. Fiber Technol.*, vol. 53, Dec. 2019, Art. no. 102043, doi: 10.1016/j.yofte.2019.102043.

[29] M. Long, P. Wang, H. Fang, and W. Hu, "Progress, challenges, and opportunities for 2D material based photodetectors," *Adv. Funct. Mater.*, vol. 29, no. 19, May 2019, Art. no. 1803807, doi: 10.1002/adfm.201803807.

[30] S. Yang et al., "High performance few-layer GaS photodetector and its unique photo-response in different gas environments," *Nanoscale*, vol. 6, no. 5, pp. 2582–2587, 2014, doi: 10.1039/c3nr05965k.

[31] S. Abubakar et al., "Fabrication and characterization of nanostructured zinc oxide on printed microcontact electrode for piezoelectric applications," *J. Mater. Res. Technol.*, vol. 9, no. 6, pp. 15952–15961, Nov. 2020, doi: 10.1016/j.jmrt.2020.11.038.

[32] S. MacKay, P. Hermansen, D. Wishart, and J. Chen, "Simulations of interdigitated electrode interactions with gold nanoparticles for impedance-based biosensing applications," *Sensors*, vol. 15, no. 9, pp. 22192–22208, Sep. 2015, doi: 10.3390/s150922192.

[33] Y. Hase et al., "Humidity sensor properties of hydrothermally grown rutile-TiO$_2$ microspheres on interdigital electrodes (IDEs)," *J. Mater. Science: Mater. Electron.*, vol. 33, no. 15, pp. 11825–11840, May 2022, doi: 10.1007/s10854-022-08146-4.

[34] Y. Zhao, B. Yang, and J. Liu, "Effect of interdigital electrode gap on the performance of SnO$_2$-modified MoS$_2$ capacitive humidity sensor," *Sens. Actuators B, Chem.*, vol. 271, pp. 256–263, Oct. 2018, doi: 10.1016/j.snb.2018.05.084.

[35] A. Mathur, S. Roy, S. Nagabooshanam, S. Wadhwa, and S. Dubey, "Effect of gap size of gold interdigitated electrodes on the electrochemical immunosensing of cardiac troponin-I for point-of-care applications," *Sensors Actuat. Rep.*, vol. 4, Nov. 2022, Art. no. 100114, doi: 10.1016/j.snr.2022.100114.

[36] S. V. Averine, Y. C. Chan, and Y. L. Lam, "Geometry optimization of interdigitated Schottky-barrier metal–semiconductor–metal photodiode structures," *Solid-State Electron.*, vol. 45, no. 3, pp. 441–446, Mar. 2001, doi: 10.1016/s0038-1101(01)00017-x.

[37] S. Averine, O. Bondarenko, and R. Sachot, "High-speed limitations of the metal-semiconductor-metal photodiode structures with submicron gap between the interdigitated contacts," *Solid-State Electron.*, vol. 46, no. 12, pp. 2045–2051, Dec. 2002, doi: 10.1016/S0038-1101(02)00165-X.

[38] C. R. Bowen, L. J. Nelson, R. Stevens, M. G. Cain, and M. Stewart, "Optimisation of interdigitated electrodes for piezoelectric actuators and active fibre composites," *J. Electroceram.*, vol. 16, no. 4, pp. 263–269, Jul. 2006, doi: 10.1007/s10832-006-9862-8.

[39] Z. Li et al., "Understanding the role of grain boundaries on charge-Carrier and ion transport in Cs$_2$AgBiBr$_6$ thin films," *Adv. Funct. Mater.*, vol. 31, no. 49, Dec. 2021, Art. no. 2104981, doi: 10.1002/adfm.202104981.

[40] Y. Hase et al., "Fabrication of $\alpha$-In$_2$Se$_3$-Based photodetector using RF magnetron sputtering and investigations of its temperature-dependent properties," *IEEE Sensors J.*, vol. 23, no. 6, pp. 5681–5694, Mar. 2023, doi: 10.1109/JSEN.2023.3239808.

[41] F. E. Faradev, N. M. Gasanly, B. N. Mavrin, and N. N. Melnik, "Raman scattering in some III-VI layer single crystals," *Phys. Status Solidi (B)*, vol. 85, no. 1, pp. 381–386, Jan. 1978, doi: 10.1002/pssb.2220850142.

[42] Y. Zhang et al., "Fabrication of a $\alpha$-In$_2$Se$_3$/Si heterostructure photo-transistor for heart rate detection," *J. Mater. Chem. C*, vol. 9, no. 25, pp. 7888–7892, 2021, doi: 10.1039/d1tc01837j.

[43] R. G. Waykar et al., "Influence of RF power on structural, morphology, electrical, composition and optical properties of al-doped ZnO films deposited by RF magnetron sputtering," *J. Mater. Sci., Mater. Electron.*, vol. 27, no. 2, pp. 1134–1143, Feb. 2016, doi: 10.1007/s10854-015-3862-x.

[44] A. Lawal, A. Shaari, R. Ahmed, and L. S. Taura, "Investigation of excitonic states effects on optoelectronic properties of $Sb_2Se_3$ crystal for broadband photo-detector by highly accurate first-principles approach," *Current Appl. Phys.*, vol. 18, no. 5, pp. 567–575, May 2018, doi: 10.1016/j.cap.2018.02.008.

[45] A. Bhorde et al., "Highly stable and pb-free bismuth-based perovskites for photodetector applications," *New J. Chem.*, vol. 44, no. 26, pp. 11282–11290, 2020, doi: 10.1039/d0nj01806f.

[46] R. Aher et al., "Solvothermal growth of $PbBi_2Se_4$ Nano-flowers: A material for humidity sensor and photodetector applications," *Phys. Status Solidi (A)*, vol. 216, no. 11, Jun. 2019, Art. no. 1900065, doi: 10.1002/pssa.201900065.

[47] Z. Jin, L. Gao, Q. Zhou, and J. Wang, "High-performance flexible ultraviolet photoconductors based on solution-processed ultrathin ZnO/Au nanoparticle composite films," *Sci. Rep.*, vol. 4, no. 1, p. 4268, Mar. 2014, doi: 10.1038/srep04268.

[48] A. Gundimeda et al., "Fabrication of non-polar GaN based highly responsive and fast UV photodetector," *Appl. Phys. Lett.*, vol. 110, no. 10, Mar. 2017, Art. no. 103507, doi: 10.1063/1.4978427.

[49] M. H. Mamat, Z. Khusaimi, M. M. Zahidi, and M. R. Mahmood, "Performance of an ultraviolet photoconductive sensor using well-aligned aluminium-doped zinc-oxide nanorod arrays annealed in an air and oxygen environment," *Jpn. J. Appl. Phys.*, vol. 50, no. 6, Jun. 2011, Art. no. 06GF05, doi: 10.1143/jjap.50.06gf05.

[50] X. Gu, M. Zhang, F. Meng, X. Zhang, Y. Chen, and S. Ruan, "Influences of different interdigital spacing on the performance of UV photodetectors based on ZnO nanofibers," *Appl. Surf. Sci.*, vol. 307, pp. 20–23, Jul. 2014, doi: 10.1016/j.apsusc.2014.03.091.

[51] E. Monroy, T. Palacios, O. Hainaut, F. Omnès, F. Calle, and J.-F. Hochedez, "Assessment of GaN metal–semiconductor–metal photodiodes for high-energy ultraviolet photodetection," *Appl. Phys. Lett.*, vol. 80, no. 17, pp. 3198–3200, Apr. 2002, doi: 10.1063/1.1475362.

[52] K. W. Liu et al., "Ultraviolet photoconductive detector with high visible rejection and fast photoresponse based on ZnO thin film," *Solid-State Electron.*, vol. 51, no. 5, pp. 757–761, May 2007, doi: 10.1016/j.sse.2007.03.002.

[53] J. Xing, H. Wei, E.-J. Guo, and F. Yang, "Highly sensitive fast-response UV photodetectors based on epitaxial $TiO_2$ films," *J. Phys. D, Appl. Phys.*, vol. 44, no. 37, Sep. 2011, Art. no. 375104, doi: 10.1088/0022-3727/44/37/375104.

[54] O. A. Abbas, C.-C. Huang, D. W. Hewak, S. Mailis, and P. Sazio, "(INVITED) opto-electronic properties of solution-synthesized $MoS_2$ metal-semiconductor-metal photodetector," *Opt. Mater., X*, vol. 13, Jan. 2022, Art. no. 100135, doi: 10.1016/j.omx.2022.100135.

[55] H.-Y. Chen et al., "Realization of a self-powered ZnO MSM UV photodetector with high responsivity using an asymmetric pair of Au electrodes," *J. Mater. Chem. C*, vol. 2, no. 45, pp. 9689–9694, 2014, doi: 10.1039/C4TC01839G.

[56] L. Goswami et al., "Fabrication of GaN nano-towers based self-powered UV photodetector," *Sci. Rep.*, vol. 11, no. 1, p. 10859, May 2021, doi: 10.1038/s41598-021-90450-w.

[57] S.-C. Kung, W. E. van der Veer, F. Yang, K. C. Donavan, and R. M. Penner, "20 $\mu$s photocurrent response from lithographically patterned nanocrystalline cadmium selenide nanowires," *Nano Lett.*, vol. 10, no. 4, pp. 1481–1485, Apr. 2010, doi: 10.1021/nl100483v.

[58] T. S. Reddy and M. C. S. Kumar, "Co-evaporated SnS thin films for visible light photodetector applications," *RSC Adv.*, vol. 6, no. 98, pp. 95680–95692, 2016, doi: 10.1039/c6ra20129f.

[59] J. D. Yao, Z. Q. Zheng, J. M. Shao, and G. W. Yang, "Stable, highly-responsive and broadband photodetection based on large-area multilayered $WS_2$ films grown by pulsed-laser deposition," *Nanoscale*, vol. 7, no. 36, pp. 14974–14981, 2015, doi: 10.1039/c5nr03361f.

[60] C. Chen et al., "Highly responsive $MoS_2$ photodetectors enhanced by graphene quantum dots," *Sci. Rep.*, vol. 5, no. 1, p. 11830, Jul. 2015, doi: 10.1038/srep11830.

[61] D. Alagarasan et al., "Influence of nanostructured SnS thin films for visible light photo detection," *Opt. Mater.*, vol. 121, Nov. 2021, Art. no. 111489, doi: 10.1016/j.optmat.2021.111489.

[62] A. S. Pawbake, R. G. Waykar, D. J. Late, and S. R. Jadkar, "Highly transparent wafer-scale synthesis of crystalline $WS_2$ nanoparticle thin film for photodetector and humidity-sensing applications," *ACS Appl. Mater. Interfaces*, vol. 8, no. 5, pp. 3359–3365, Feb. 2016, doi: 10.1021/acsami.5b11325.

[63] P. Hou et al., "Ionization effect and displacement effect induced photoresponsivity degradation on $\alpha$-$In_2Se_3$ based transistors for photodetectors," *Radiat. Phys. Chem.*, vol. 174, Sep. 2020, Art. no. 108969, doi: 10.1016/j.radphyschem.2020.108969.

[64] R. K. Mech, S. V. Solanke, N. Mohta, M. Rangarajan, and D. N. Nath, "$In_2Se_3$ visible/near-IR photodetector with observation of band-edge in spectral response," *IEEE Photon. Technol. Lett.*, vol. 31, no. 11, pp. 905–908, Jun. 1, 2019, doi: 10.1109/LPT.2019.2912912.

[65] H. A. Khizir and T. A.-H. Abbas, "Hydrothermal growth and controllable synthesis of flower-shaped $TiO_2$ nanorods on FTO coated glass," *J. Sol-Gel Sci. Technol.*, vol. 98, no. 3, pp. 487–496, Jun. 2021, doi: 10.1007/s10971-021-05531-z.

[66] N. Prakash et al., "Ultrasensitive self-powered large area planar GaN UV-photodetector using reduced graphene oxide electrodes," *Appl. Phys. Lett.*, vol. 109, no. 24, Dec. 2016, Art. no. 242102, doi: 10.1063/1.4971982.

[67] M. Talib et al., "Development of ultra-sensitive broadband photodetector: A detailed study on hidden photodetection-properties of $TiS_2$ nanosheets," *J. Mater. Res. Technol.*, vol. 14, pp. 1243–1254, Sep. 2021, doi: 10.1016/j.jmrt.2021.07.032.

[68] S. Kumar et al., "Development of transition metal dichalcogenides for modern photodetector devices," in *Proc. Int. Conf. Inf. Technol. Nanotechnol. (ITNT)*, Sep. 2021, pp. 1–4, doi: 10.1109/ITNT52450.2021.9649438.

[69] M. Hasani, S. Hamedi, and H. Dehdashti Jahromi, "Experimental and theoretical analysis of a visible-light photodetector based on cadmium sulfide fabricated on interdigitated electrodes," *Results Phys.*, vol. 56, Jan. 2024, Art. no. 107291, doi: 10.1016/j.rinp.2023.107291.

[70] J. Ferrer, J. Alonso, and S. De Ávila, "Electrical characterization of photodetectors based on poly(3-hexylthiophene-2,5-diyl) layers," *Sensors*, vol. 14, no. 3, pp. 4484–4494, Mar. 2014, doi: 10.3390/s140304484.